FEBIP for Functional Nanolithography of 2D Nanomaterials

Songkil Kim[1] and Andrei G. Fedorov[2,3,*]

[1]School of Mechanical Engineering, Pusan National University, Busan 46241, South Korea

[2]George W. Woodruff School of Mechanical Engineering, Georgia Institute of Technology, Atlanta, GA 30332, USA

[3]Parker H. Petit Institute for Bioengineering and Bioscience, Georgia Institute of Technology, Atlanta, GA 30332, USA

*Corresponding Author: agf@gatech.edu

Abstract

Lithographic patterning on emerging nanomaterials is one of essential ingredients for the development of new functional nanomaterial and device systems. Focused electron beam induced processing (FEBIP) in combination with an on-demand reconfigurable precursor injection system enables the highest resolution and controllability of nanolithography on two-dimensional (2D) nanomaterials. FEBIP allows for localized atomic-to-nanoscale engineering of nanomaterials and devices in a multi-mode format including geometrical patterning, functionalization/defect formation/doping, metal/metal oxide deposition, interface fusion and activation, active channel cleaning. This chapter discusses the scientific bases and showcases the state-of-the-art FEBIP technologies with a specific focus on functional lithography of 2D nanomaterials and provides future prospects of FEBIP technologies to address real industrial needs for the development of high-performance, next-generation functional devices.

X.1. Introduction

Localized manipulation of nanomaterials can provide unprecedented opportunities for design of new functionalities as well as breakthrough improvements of existing properties of nanomaterials. Having a high degree of control with atomic-to-nanoscale resolution, a focused electron beam with a broad energy range in combination with molecular precursors delivered locally in an electron microscope environment is a promising imaging probe and a powerful “direct write” tool enabling local excitation and modification of nanomaterials. Focused electron beam induced processing (FEBIP) is a next-generation technology for a *nanofactory* where

deposition, etching, fusion, doping and other manipulations of nanomaterials occur in a multi-mode format and is simultaneously combined with ultra-high-resolution *in-situ* imaging to provide unique opportunities in new materials design and analysis.

Two-dimensional (2D) nanomaterials have been extensively explored owing to their unique mechanical, optical, thermal and electrical properties [1]. Atomically thin 2D layered materials have been a subject of much attention after the successful mechanical exfoliation of graphene from graphite by Novoselov and Geim [2]. Graphene is a single atom-thick hexagonal carbon structure, which is optically transparent and has ultra-high carrier mobility, high thermal conductivity and Young's modulus at room temperature [1]. The discovery of graphene with its extraordinary properties motivated exploration of other 2D nanomaterials, including an insulating 2D hexagonal boron-nitride (h-BN) and especially 2D inorganic semiconducting nanomaterials with non-zero electronic bandgaps [1]. Transition metal dichalcogenides (TMDs) are layered materials with a stoichiometry of MX_2 where M is transition metals, including Mo, Ti, Ta, and W, and X is chalcogens, such as S, Se and Te. In particular, a single-layer MoS_2, a direct band gap semiconductor, has been under intense attention since it can be a component for flexible high-performance 2D electronics and optoelectronics and can also be stacked with semi-metallic graphene and insulating h-BN to form a van der Waals heterostructure for novel functional devices [3]. Owing to the tunable nature of 2D nanomaterials' properties, they present an interesting platform as a model multi-layer nanomaterial for application of FEBIP capabilities for site-specific, high-resolution modification of the composite interface formation and modulation of interfacial and transport properties. This chapter provides an overview of FEBIP as a direct-write lithography toolbox to atomically engineer the topological, structural and compositional features of 2D composite nanomaterials with an aim to introduce new functional properties and devices. It presents the background on atomic manipulation of 2D nanomaterials, with in depth focus on electron-beam-assisted surface doping, defect formation, etching, interface fusion and examples of FEBIP applications to 2D nanomaterial-based electronic devices.

X.2. Atomic Manipulation of 2D Nanomaterials

X.2.1. Defect Engineering of 2D Nanomaterials

Directed atomic manipulation of 2D nanomaterials can be achieved using a focused electron beam in (scanning) transmission electron microscopy. A large number of *in-situ* experiments have been conducted to investigate electron beam irradiation effects on atomic structures of 2D nanomaterials along with atomic-resolution imaging [4, 5]. High energy focused electrons transfer energy to 2D nanomaterial systems so that controllable defect formation can be achieved by tuning beam parameters such as energy, current, irradiation time/area and the corresponding electron beam dose. Defects can deteriorate the mechanical and electronic properties of pristine nanomaterials in general, but they can also enhance chemical and magnetic properties or impose new functional properties to nanomaterials. Thus, controlling the formation of specific defects using an electron beam at atomic resolution will provide a unique opportunity for structure-induced tuning of materials' properties.

Typical point defects in graphene include sp^3-type defects, Stone-Waals defects and vacancy formation [6]. They can be formed by electron irradiation at varying levels of beam accelerating energy. An sp^3-type defect is defined as sp^3-hybridization appearing locally so that new covalent bonds can be formed between adatoms and the underlying carbon atoms in the graphene basal plane, which can be induced by mild electron irradiation at a relatively low energy in a range of a few tens of keVs. The energetically favored adsorption configuration of adatoms is the bridge site over the top of carbon-carbon bond of graphene having a binding energy of 1.5 – 2 eV [6]. Other metastable configurations are feasible and the energy difference between different configuration states is as small as ~0.3 eV, which indicates that the adatoms are very mobile over the graphene plane and can be stimulated to migrate by the external energy input such as electron irradiation or do so spontaneously due to thermal fluctuations even at room temperature [6]. The adatoms can be carbon atoms from e-beam dissociated hydrocarbons adsorbed on the surface (e.g., from surface contamination) or other foreign atoms introduced onto a surface, e.g., via FEBID. The adatom can change properties of graphene depending on whether it strongly interacts with graphene or not. Electron irradiation can activate the chemical interactions of foreign adatoms and graphene, which establish new functionality and/or modify the intrinsic properties of graphene.

Stone-Waals (SW) defects result from the rotation of one carbon-carbon bond at an in-plane 90° with no removal or displacements of carbon atoms [6-8]. Figure 1(a) shows the calculated energy barrier for bond rotation. The kinetic barrier for the formation of the SW defect is about 9–10 eV and the energy barrier for the reverse bond rotational transformation is 5 eV, indicating that the SW defect is quite stable at room temperature [7]. Due to the high kinetic barrier, it can be rarely found in an equilibrium state after graphene synthesis that typically occurs at temperatures below 1000 °C. However, electron irradiation can lead to the non-equilibrium change of local states of graphene and an electron beam at an accelerating energy less than 80 keV can form SW defects with no vacancy formation [6]. Figures 1(b)-1(d) show the atomic model demonstrating the C-C bond rotation to form the SW defect, and the corresponding aberration-corrected TEM image of the SW defect is shown in Fig. 1(e).

Vacancy formation occurs by direct sputtering of carbon atoms from the lattice by high energy electron beam irradiation. The threshold energy for knock-on displacements of carbon atoms in graphene is 18–22 eV, which can be transferred by electron impact at an accelerating energy higher than 90 keV, based on the theoretical estimations [4, 6]. Figures 1(f)-1(k) shows atomic models of single vacancy (SV) and divacancy (DV) defects and the corresponding TEM images. Vacancies are unstable due to the dangling bonds which can lead to the reconstruction of defected sites and attract carbon adatoms or other foreign elements to passivate the edges of graphene or to form a perfect graphene lattice under electron irradiation. Prolonged electron beam irradiation can result in sequential removal of carbon atoms, but also facilitate the transformation of defected graphene into more stable structures. Vacancy formation can also occur with the intense beam current density (corresponding to the increased electron beam dose) at an electron beam energy of 80 keV, lower than a threshold electron beam energy theoretically estimated [4]. Electron accelerating energy of 80 keV is not sufficient to result in direct knock-on sputtering of carbon atoms by electron impingement, but any adatom under electron beam irradiation can interact with graphene disrupting the sp^2 hexagonal network and weakening the binding of C-C bonds [4]. In addition, the prolonged electron beam irradiation transits any perturbation to pristine graphene, including SW defects and

interstitials, to vacancy formation since the C-C bond strength of graphene becomes weakened and thus, the threshold displacement energy of carbon atoms can be lowered [4-6]. Defect formation on graphene is a very complex process, and many different types of defects such as point defects, line defects (dislocations) and phase transformation to 2D amorphous structures can occur sequentially and concurrently. Annealing and quenching of existing defects, while new defects are being formed under electron beam irradiation, make it difficult clearly define the contributions of electron beam conditions to defect evolution and properties in graphene, unless the electron irradiation conditions are set with the sufficient beam energy and dose to exceed the threshold limits for generating a certain type of defects.

Defects in graphene can be reactive sites to attract functional elements and build up a composite material system whose activation energy can be easily overcome under electron beam irradiations. For example, surface Fe residual atoms driven by electron beam irradiations are structured to a freestanding Fe monolayer in suspended graphene nanopores for the enhanced magnetic moment [9]. The low-voltage spherical aberration-corrected TEM was utilized as a platform to image and irradiate graphene with Fe residual atoms with the electron beam energy of 80 keV. The fast Fourier transformation of the TEM image verified the Fe crystal lattice structure formed within the graphene nanopore along with the atomic model by the density functional theory (DFT) calculation.

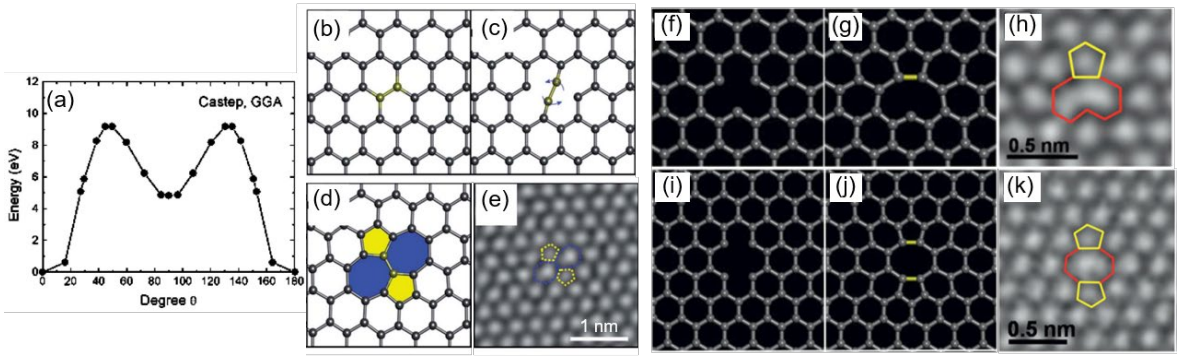

Figure 1. (a) DFT calculations of formation energies for C-C bond rotations depending on angles showing that a SW defect can be generated by overcoming an energy barrier of ~10 eV. (Reprinted with permission from [7], Copyright (2005) by the American Physical Society) (b)-(d) Atomic models and (e) the corresponding aberration-corrected (AC) TEM image to describe the bond rotations to form a SW defect. (Reproduced from [8] with permission of The Royal Society of Chemistry) (f), (g) Atomic models of a mono vacancy formation describing a single carbon atom sputtered and the structural relaxation to a final form of a monovacancy (5-9), which is identical to the (h) AC TEM image. (i),(j) Atomic models of the divacancy (5-8-5) formation with (k) the corresponding AC TEM image. (Reproduced from [4] with permission)

Beyond the graphene, many different types of 2D nanomaterials including hexagonal boron nitride (h-BN) and transition metal dichalcogenides (TMDs) have been explored for local modification by focused electron beam

irradiation. Bi-component 2D nanomaterials under electron beam irradiation provide many intriguing opportunities for new functionalities and designs, which include atomic fabrication of heterogeneous structures and directed phase patterning. h-BN is an insulating 2D nanomaterial which has the closest structural similarity to graphene [4, 10]. The difference in the threshold energy for knock-on displacements between B atoms (74 keV) and N atoms (84 keV) enables the selective sputtering or displacements of B atoms under the controlled electron beam irradiation conditions [11]. High energy electron beam can perforate a h-BN monolayer to replace sputtered B or N atoms with carbon atoms formed by e-beam induced dissociation of surface adsorbed hydrocarbons, which creates a new composite BCN 2D nanomaterial [10].

Many 2D transition metal dichalcogenides nanomaterials were extensively explored to study electron beam induced production of defects by calculating the displacement threshold energy for sputtering an atom using the density functional theory (DFT) calculations, which concluded that chalcogenides atoms are more easily sputtered rather than transition metals [12]. The displacement threshold energies of chalcogenides atoms were calculated ranging between ~3.5 eV and ~7.2 eV for $TaTe_2$ and TaS_2, respectively. One of the representative transition metal dichalcogenides nanomaterials is molybdenum disulfide (MoS_2). It is a three-atom-thick semiconducting nanomaterial at the energetically stable semiconducting phase, which can, however, have multiple metastable phases with different electronic properties [13]. Electron beam irradiation can lead to the selective sputtering of sulfur atoms due to the lower threshold energy for the atomic displacement than that for the molybdenum atoms. Sulfur atoms can be knocked out with an electron energy at 80 keV or higher [5, 12]. Vacancy formation and bond rotation result in diverse defect types, and six representative point defects can be induced in a monolayer MoS_2 by electron beam irradiation, including a monosulfur vacancy, a disulfur vacancy and an anti-site defect in which a Mo atom substitutes a S_2 column [5]. Line defects are the extended defects as the agglomeration of vacancies, which can be controllably patterned under electron beam irradiation [5, 14, 15]. Grain boundary is also one of line defects in MoS_2, which can be mirror and tilt twin boundaries as can be revealed by photoluminescence (PL) images, and the increased conductance was measured in the current flow direction parallel to the grain boundary [14]. Line defects can provide local conductive paths in a semiconducting matrix and some line defects were theoretically proven to have a magnetic property. Importantly, the electronic band gap reduces with the increased number of line defects, as shown in Fig. 2, which can be “inserted” by the highly controllable electron beam irradiation to develop novel functional devices [15].

Another interesting characteristic of MoS_2 is that it has two primary phases: 2H semiconducting and 1T metallic phases. High-energy electron beam irradiation can induce the transformation of its phase from the stable 2H phase to the metastable 1T phase [13]. Sufficient charge accumulation in 2H semiconducting MoS_2 under electron beam irradiation in the STEM environment led to the transformation of the phase by gliding the lattice-plane of sulfur. The local phase transformation and of MoS_2 in electronic device applications enables low-resistant MoS_2-metal contacts, and it can realize the development of high-performance, low-powered MoS_2-based electronic devices. In addition, nanosculpturing of 2D MoS_2 using the focused electron beam can fabricate a conductive nanowire [16]. Figure 3(a) shows the fabrication of a MoS nanowire from a single layer MoS_2 by directed electron beam irradiation. Two nanoholes were first fabricated on a suspended MoS_2, and scanning the

electron beam over the bridge between two holes continuously thinned the nanowire at the atomic precision. The thinner nanowire was measured to have higher electrical conductivity as shown in Figs. 3(b) and 3(c).

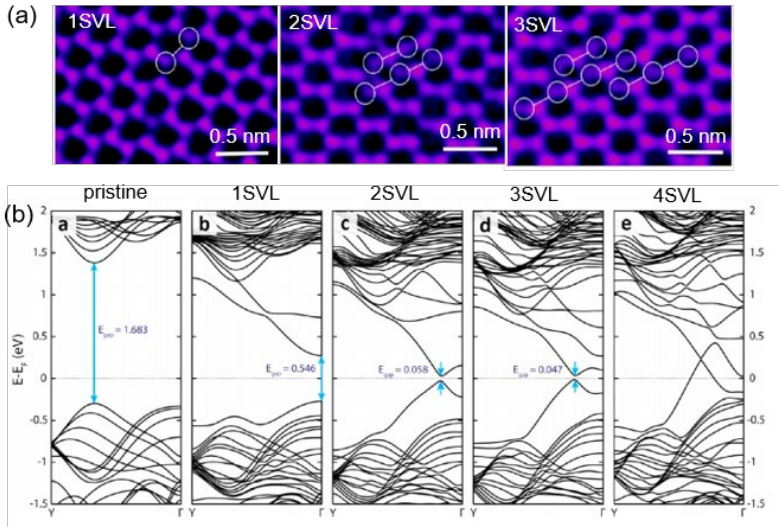

Figure 2. (a) STEM images of short single-vacancy line defects (1SVL, 2SVL and 3SVL) generated by electron beam irradiation, (Adapted with permission from [15]. Copyright (2016) American Chemical Society) and (b) the corresponding electronic band structures highlighting the reduction of the band gap energy with the increase in the number of line defects indicative of the transition from semiconducting to metallic phases. (Reprinted with permission from [15]. Copyright (2016) American Chemical Society)

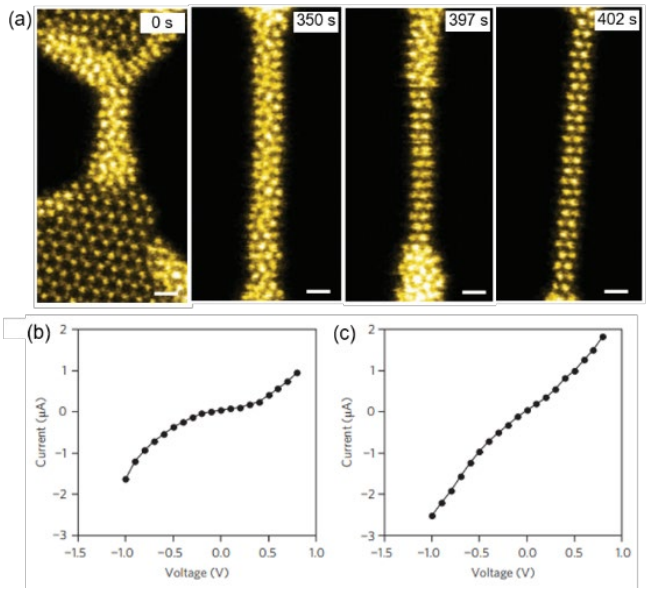

Figure 3. Fabrication of a nanowire from a single layer 2D MoS_2 using 60 keV electron beam irradiation in the

STEM environment. (a) False-colored STEM images showing the reduction of the nanowire widths under electron beam irradiation, and the electrical measurement (*I-V* curves) results for (b) a relatively thick nanowire and (c) a further thinned nanowire, demonstrating the increase of conductivity. (Reprinted by permission from Springer Nature Customer Service Centre GmbH: Springer Nature, Nature Nanotechnology [16], Copyright (2014))

X.2.2. Directing Matter: Atomic Forging with *In-situ* Imaging and Material Manipulations

The advances in electron microscopy and computing power have brought new opportunities in materials design and imaging at atomic-to-nanoscales, bringing Feynmann's vision of forming the functional micro/nano-systems via atom-by-atom addition/removal of material into a reality with some recently demonstrated remarkable examples. Aberration-corrected scanning transmission electron microscopy (STEM) enables atomically-resolved imaging of materials with its focused electron beam as a probe whose size is ~0.1 nm. Energetic focused electron beam with an atomic diameter can locally excite atoms of materials to manipulate into programmed locations and to build molecular structures. Local interaction of electrons with solid state matters has been explored to verify feasibility of material manipulations in atomic scales, enabling a true bottom-up synthesis of nanomaterials. A vision of fully automated, atomic scale fabrication of nanomaterials, called "atomic forge," was recently suggested to tune material properties in a programmed manner [17]. The "atomic forge" requires the advancement of electron beam control, real-time monitoring and image data analytics, and swift feedback to control the beam. Recently, much effort has been on the development and demonstration of real atomic fabrication and image data processing [18-21].

Susi *et al.* first demonstrated that 60 keV electron irradiation can cause structural rearrangements at silicon dopant sites in the graphene lattice which undergo a random walk due to structural relaxation with the mechanism described in Fig. 4(a) [18]. Molecular dynamic simulation of electron impact delivering 15 eV to a carbon atom neighboring Si-C_3. The ejected C atom travels slightly away and then towards the Si atom. While the Si atom falls under relaxation into the vacated carbon site, the ejected carbon atom is drawn back to the position of the starting point of the Si atom [18]. After the first demonstration of a possibility for atomic manipulation under electron beam irradiation, they recently conducted the very detailed study about single-atom dynamics of phosphorus dopants on graphene under selective electron beam irradiation using the experiments and the first-principles calculations [20]. An underlying theory was developed to estimate the probabilities of atomic configurational transformations. The researchers in the Oak Ridge National Laboratory first demonstrated the directed displacements of a Si atom in graphene lattice [19]. Parking a focused electron beam in the next lattice site of the target dopant (silicon atom) drives the movement of the silicon atom to the site under electron irradiation at the beam energy of 60 keV. They demonstrated the linear motion of a silicon atom (Fig. 4(b)) as well as formation of dimer (Fig. 4(c)) and trimer and their rotational motion, along with silicon atom manipulation at the edges of a graphene hole for passivation and de-passivation. To provide better understanding of the dynamics of dopant atoms on graphene, a deep learning network was applied to analyze low-resolution STEM movies and to extract atomic configurations and coordinates of carbon and silicon atoms enabling the study of electron beam-

induced chemical transformations at the edge and in the bulk of graphene [21]. Many technological challenges still remain to be solved before the atomic forging of nanomaterials can be applied to realize operational functional devices on a large scale, but continuous development of instrumentation, theory and data science such as artificial intelligence and machine learning will significantly accelerate the realization of true atomic manufacturing of new functional nanomaterials, structures and devices.

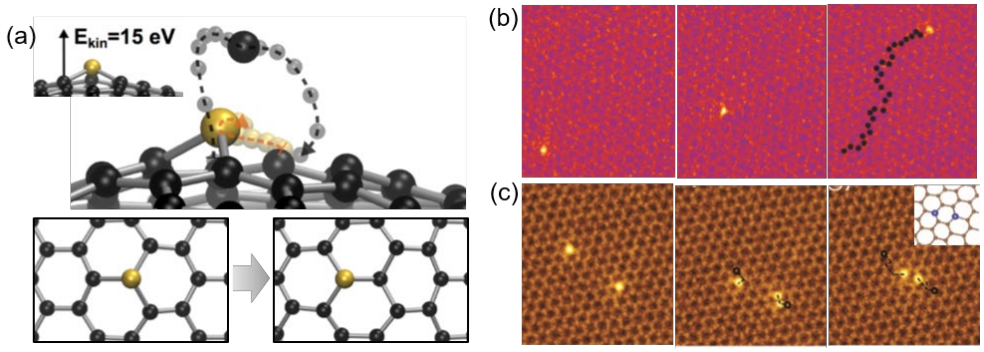

Figure 4. (a) Molecular dynamic simulation result demonstrating the mechanism for electron beam induced displacement of a Si dopant from one atomic position to the next neighboring position in graphene lattice structure. (Reprinted with permission from [18], Copyright (2014) by the American Physical Society) (b) STEM images showing the electron beam-induced atomic linear motion of a Si dopant on graphene along a path length of ~4 nm and (c) the formation of a Si dimer by manipulating two Si atoms using the electron beam. ([19] John Wiley & Sons. © 2018 WILEY-VCH Verlag GmbH & Co. KGaA, Weinheim)

X.3. Directed Surface and Interface Modification of Graphene-Based Nanomaterials Using Focused Electron Beam and Precursor Molecules

Scanning electron microscopy (SEM) environment enables nanoscale-to-microscale manipulation of 2D materials with a large electron beam size (few nanometer) and lower accelerating voltages from few hundreds electron volts (eV) to 30 keV. Single atomic manipulation of 2D nanomaterials cannot be realized at such relatively low voltages, but advantageously a larger area patterning and fabrication of operational devices can be achieved using the SEM beams in combination with directed introduction of molecular precursors to the beam irradiation site. Nanoscale resolution of 2D nanomaterial patterning and the corresponding functional mapping of nanoelectronic devices can be accomplished, where, otherwise, multiple steps are required and uncontrollable damage or undesired contamination of graphene substrate can occur when using the conventional lithographic techniques.

X.3.1. Graphene Oxide

An intriguing characteristics of graphene is its 2D structure which can be chemically modified, so as to endow new functional properties to a baseline material or its derivatives. One representative form of graphene-based nanomaterials is graphene oxide, whose 2D graphitic structure has surface functional groups such as epoxy, hydroxyl and carboxyl [22]. Depending on the content of surface functional groups, graphene oxide can be an insulator or a semiconductor. The conventional bulk synthesis method of graphene oxide makes ~70% of surface functional groups to the number of carbon atoms in graphene which is an insulator, and then graphene oxide is reduced to have conductivity and controllable electronic bandgap [22]. Conventional methodologies for reduction of graphene oxide are to utilize toxic chemicals and a high temperature thermal process, which are not environment-friendly and can damage electronic device substrates [23]. Moreover, patterned reduction of graphene oxide requires multiple steps of lithography procedures, which are time-consuming and often result in additional defects or contaminations. Kim *et al.* developed a direct-write method using a focused electron beam in the SEM environment for nanoscale patterned reduction of graphene oxide with no need for toxic chemicals and multiple lithographic steps [24]. As shown in Figs. 5(a) and 5(b), they fabricated a graphene oxide device on a SiO_2/Si substrate, whose channel was simply irradiated by focused electron beam at the energy of 25 keV and the dose in the order of 10^{17} to 10^{18} electrons/cm^2. No current was measured through the insulating graphene oxide before irradiation, but after electron beam irradiation, the current started to flow through graphene oxide and it increased with the increase of the electron beam dose for irradiation, as shown in Fig. 5(c). The density function theory (DFT) calculations demonstrated the likely mechanism underlying the experimental observation of the electron beam induced nanoscale reduction of graphene oxide. Hydrocarbon contamination molecules omnipresent on graphene oxide were dissociated by secondary electrons generated by inelastic collisions of primary electrons with the graphene oxide/supporting substrate. The dissociated hydrocarbon or carbon species interacted with graphene oxide to take epoxy or hydroxyl groups from graphene oxide, which finally reduced graphene oxide.

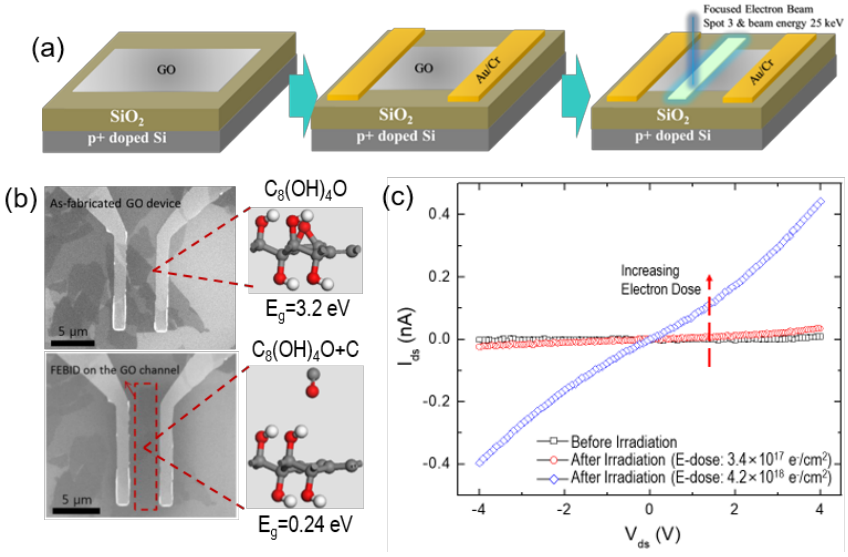

Figure 5. (a) Schematic describing the focused electron beam-induced selective reduction of graphene oxide in a device structure. (b) The SEM images of a graphene oxide device before and after the e-beam induced reduction at the channel area with the insets showing the atomic models of graphene oxide and locally reduced graphene oxide. (c) Electrical measurements of the graphene oxide device as a function of the electron dose, as compared to as-fabricated device without electron irradiation, indicating the increase of the channel conductivity with electron irradiation. (Reprinted from [24], with the permission of AIP Publishing)

X.3.2. Other Members of Graphene-Based Nanomaterials

In addition to graphene oxide, graphene functionalization was extensively studied with elements such as hydrogen, fluorine, and carbon for tuning properties of graphene [25-27]. The focused electron beam enables selective, nanoscale surface functionalization or de-functionalization of graphene-based nanomaterials. Surface functionalization of graphene under electron beam irradiation requires the introduction of precursor molecules containing a target element to be chemically attached to a graphene basal plane [25]. Interaction of electron-graphene-precursor molecules entails the excitation of graphene structure with a high energy electron beam and the dissociation of precursor gas molecules adsorbed on graphene with the secondary electrons generated as the results of interaction between the primary focused electron beam and the graphene/substrate. Fully hydrogenated graphene is called “graphane”, which has a wide bandgap tunable depending on the extent of hydrogenation. At some extents of hydrogenation, hydrogenated graphene can exhibit ferromagnetism, and the magnetic properties of hydrogenated graphene are especially useful in applications such as information technology and superconducting quantum devices [28, 29]. To controllably hydrogenate graphene using electron beam, NH_3 and water molecules were tested in ultra-high vacuum conditions and micro Raman spectroscopic analysis were implemented to evaluate the formation of hydrogenated graphene under electron beam irradiation with different energies (100 eV – 10 keV) and electron doses (2.8 mC/cm^2 – 210 mC/cm^2) [25]. Being supported by the control experiments with other gases (O_2, Ar, N_2, H_2, and CO_2), it was concluded that the electron beam-induced dissociation of the adsorbed NH_3 and H_2O molecules on graphene played a significant role to produce H^+ ions and H radicals for the formation of fully or partially hydrogenated graphene [25]. Figure 6(a) shows the Raman spectra of graphene irradiated by an electron beam at an energy of 5 keV and a dose of 1.2 mC/cm^2 after exposing graphene to various gases. The appearance of a D-band peak in the Raman spectra of graphene with NH_3 and H_2O gases confirms the hydrogenation of graphene compared to the results of no D-band peak appearance in the spectra with other gases. Hydrogen gas molecules are difficult to adsorb on graphene and thus, not suitable as a direct route to hydrogenation.

Other studies used a hydrogen silsesquioxane (HSQ) film, which is a negative photoresist for e-beam lithography, as a source of hydrogen [28, 30]. Breaking a bond of Si-H of the HSQ film produced hydrogen radicals to be chemically bound to a graphene basal plane forming a hydrogenated graphene. Hydrogenated graphene under electron beam irradiation can be reversibly dehydrogenated by thermal annealing at the relatively low temperature of ~ 200 °C [30]. A weakly hydrogenated graphene was proven to have the enhanced spin-orbit

coupling which can overcome the limitation in graphene's applications due to extremely small spin-orbit interactions [28]. HSQ was used to hydrogenate graphene under electron beam irradiation. The localized patterning of graphene hydrogenation using electron beam is beneficial to precisely control the process without introducing undesired vacancies, compared to the bulk, destructive radio frequency (RF) hydrogen plasma process. Figures 6(b)-6(d) show the results of the enhanced spin-orbit coupling of the hydrogenated graphene device selectively patterned by electron beam irradiation and the hydrogenation revealed by Raman measurements depending on electron beam energies and doses [28]. The focused electron beam was also used to pattern magnetic regions in hydrogenated graphene by selectively removing hydrogen atoms and quenching the magnetism to generate non-magnetic graphene domains [29]. Figures 6(e) and 6(f) shows the patterned magnetic array of partially hydrogenated graphene which was imaged using magnetic force microscopy (MFM).

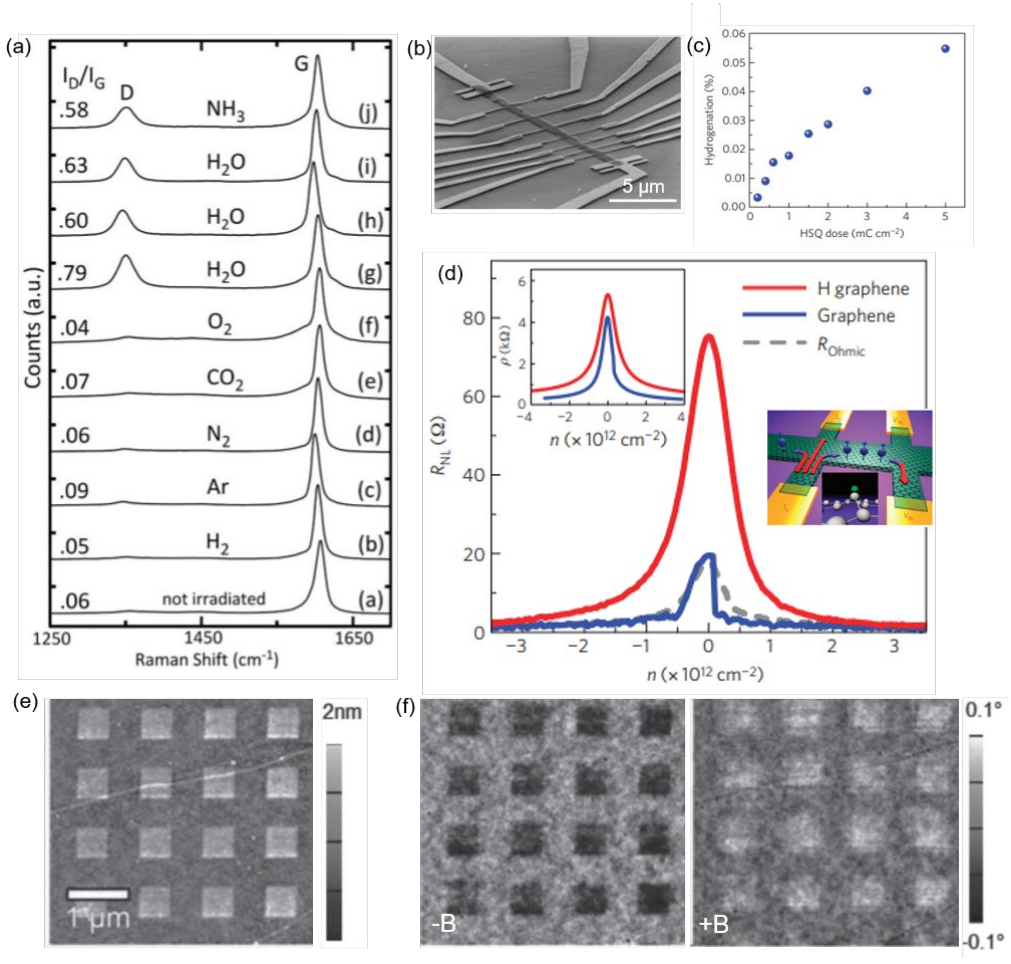

Figure 6. (a) Raman spectra of graphene under electron beam irradiation with a variety of precursor gases, which demonstrating that water and NH3 gases can be a precursor source for hydrogenation of graphene. (Reprinted from [25], Copyright (2010), with permission from Elsevier) (b) SEM image of a partially hydrogenated graphene device showing multiple Hall bar junctions and (c) evolution of the hydrogenation on graphene by increasing the

electron dose from 0.4 to 5 mC/cm^2 for HSQ dissociation. (d) Room temperature measurements of non-local signal (R_{NL}) depending on charge densities (n) for partially hydrogenated (~0.02%) graphene (red) and a pristine graphene (blue) highlighting that even weak hydrogenation of graphene enhanced the spin-orbit coupling by ~400% compared to the pristine graphene device. The insets show the resistance measurements on charge densities and the measurement schematics for non-local spin Hall measurement with the atomic structure of a partially hydrogenated graphene. (Reprinted by permission from Springer Nature Customer Service Centre GmbH: Springer Nature, Nature Physics [28], Copyright (2013)) (e) Surface topography image of the partially hydrogenated square pattern (500 nm × 500 nm) array which was generated on a fully hydrogenated graphene surface by means of dehydrogenation using an electron beam patterning, and (f) the corresponding MFM phase images with a tip magnetized with the south pole (-B) and with the north pole (+B), indicative of magnetism on the square pattern array of partially hydrogenated graphene. ([29] John Wiley & Sons. © 2015 WILEY-VCH Verlag GmbH & Co. KGaA, Weinheim)

Fluorinated graphene is a stable, wide-bandgap nanosheet, whose carbon atoms are covalently bonded to F atoms [31]. It is an emerging member of graphene family owing to its unusual properties, including a large negative magnetoresistance, a wide optical bandgap (3.8 eV) and an ultra-high room-temperature electrical resistance, which allows for fabrication of an atomically-thin 2D insulator [26, 31, 32]. Since the properties of fluorinated graphene strongly depends on the ratio of F to C atoms, it is important to control with fine degree the level of fluorination for achieving the desired behavior. Focused electron beam irradiation tunes the properties of fluorinated graphene by local de-fluorination on exposure to electron doses (0 – 100 mC/cm^2) at the accelerating voltage of 10 keV and the beam current of 0.13 nA as shown in Fig. 7(a) [32]. The temperature dependence of the square resistance of fluorinated graphene was investigated following irradiation with different electron doses, as shown in Fig. 7(b). Increasing the electron dose reduced the coverage of F atoms on graphene from its initial composition $CF_{0.28}$ which was an insulating with a square resistance of ~1 TΩ. De-functionalization of fluorinated graphene under electron beam irradiation resulted in the decrease of electronic bandgap, converting the fluorinated graphene from insulating (no electron irradiation) to metallic (exposed to electron dose~1 C/cm^2) materials. After the irradiation at the dose of 60 mC/cm^2, the fluorinated graphene showed the characteristics of a lightly doped semiconductor. The insulating fluorinated graphene flake was used in a device configuration by depositing source and drain metal contacts and patterning a conductive channel to various widths by selectively exposing fluorinated graphene to the electron beam. This led to de-fluorination by selective fragmentation of C-F bonds, as revealed with AFM topography imaging and *I-V* measurements [26]. The electron beam induced de-fluorination ultimately transforms the insulating fluorinated graphene to pristine graphene reversibly and demonstrates the capability of controlled electron beam patterning to fabricate local, conductive channels in an insulating fluorinated graphene.

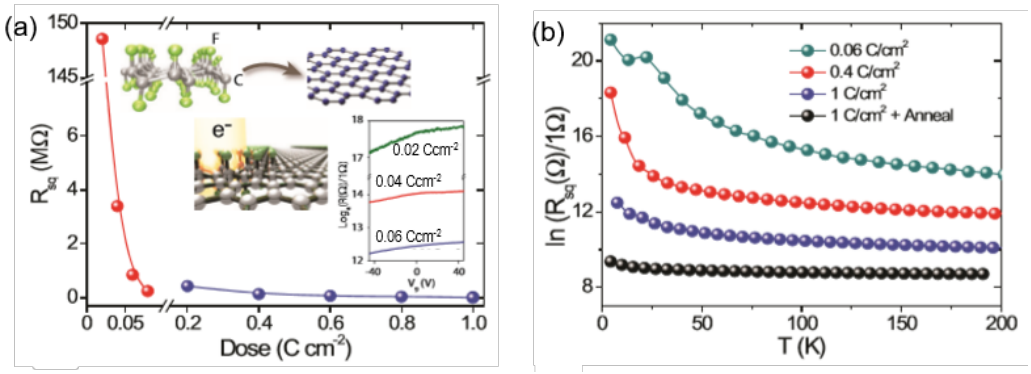

Figure 7. Controlled fluorination on graphene by electron beam irradiation. (a) The reduction of fluorinated graphene device electrical resistance upon the increase of electron beam irradiation dose as a result of defluorination (dissociating F atoms from graphene surface) and (b) the temperature dependence of the sheet resistance of fluorinated graphene subject to the electron beam irradiation with different doses, demonstrating a transition from an insulating state of $CF_{0.28}$ to a metallic state after the complete defluorination at 1 C/cm^2 followed by the mild thermal annealing to remove contaminants. (© IOP Publishing. Reproduced from [32] with permission. All rights reserved)

Another interesting members of graphene-based nanomaterials include carbon-adsorbed graphene. DFT calculations using the Vienna *ab initio* simulation package (VASP) were performed to model carbon-adsorbed graphene with various carbon coverages ranging from 3.1 % to 50 % and calculate adsorption energies, electronic structures and magnetic properties, as shown in Fig. 8(a) [27]. At the bridge site (on top of C-C bond of graphene) which is the most stable adsorption site of a carbon adatom, graphene was found to have a magnetic moment of ~0.36 μ_B per adsorbed carbon adatom at the coverages of 3.1 % and 12.5 %, while pristine graphene is non-magnetic. The further increase of the carbon adatom coverage up to 50 % changes the adsorption site to the top of carbon atoms on graphene, having no magnetic moment, but opening a band gap of 2.5 eV. Experimental implementation of carbon adsorption on graphene can be realized using focused electron beam induced deposition (FEBID) [33]. Hydrocarbon molecules physisorbed on graphene surface can be dissociated by the secondary electrons, and chemisorption of dissociated hydrocarbon species simultaneously occurs on the sp^3-type defect sites on graphene which are induced by being exposed to high energy (25 keV) primary electrons [33]. Simplified descriptions of the chemisorption phenomena were demonstrated with a model hydrocarbon molecule of CH_4, using the DFT calculations, showing the transitions of adsorption configurations when hydrogen atoms are sequentially dissociated by the secondary electrons, as shown in Fig. 8(b). The DFT calculations were confirmed with experimental measurements of two different adsorption states, physisorption *vs.* chemisorption, of hydrocarbon species on graphene. The primary electrons played a role to induce chemisorption, while the graphene areas only exposed to the secondary electrons have physisorbed carbon deposits, as shown in the Raman D-band peak mapping of Fig. 8(c). After FEBID, a molecularly thin layer of chemisorbed carbon deposits was achieved by Raman laser-assisted postdeposition thermal ablation, whose thickness was measured as ~0.8 nm by atomic force microscope (AFM), shown in Fig. 8(d), and the Raman I(D)/I(G) ratios upon thermal ablation in Fig.

8(e) confirm the chemisorption at the region where the primary electrons irradiated in contrast to the physisorption at the region where only secondary electrons contributed to deposit carbons. This study exhibits the dual capability of FEBID to make chemical functionalization of graphene as well as establish weak electronic coupling (doping) with carbon atoms.

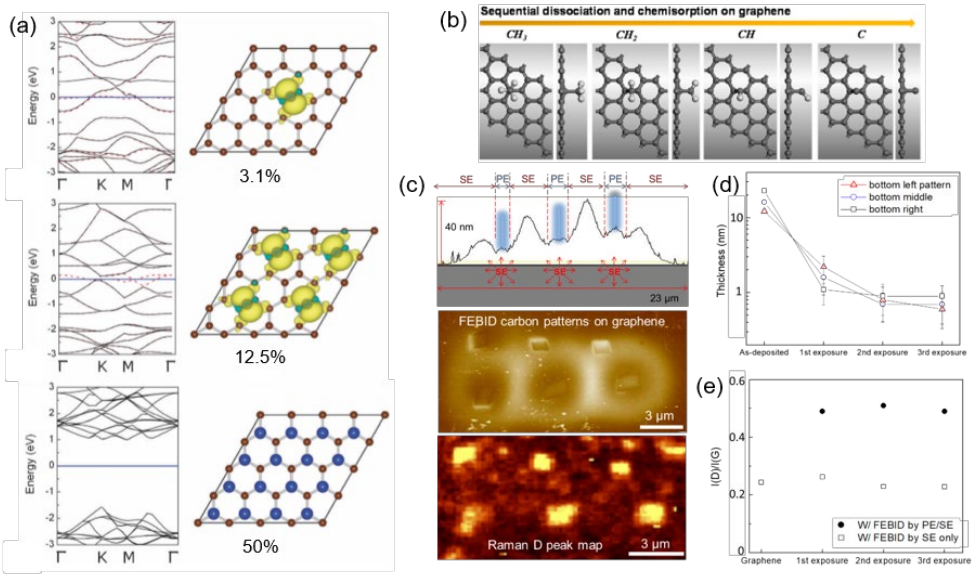

Figure 8. (a) DFT calculations of electronic band structures and adsorption configurations of carbon adatoms on graphene depending on the carbon coverage (3.1% - 50%), showing that carbon adsorbed graphene at a low surface coverage can have a magnetic property while a high surface coverage about 50% can open up the electronic band gap in graphene. (Reproduced from Ref. 27 with permission from the PCCP Owner Societies) (b) DFT calculations for describing an atomic mechanism of the FEBID process of a simple model of a CH_4 molecule on graphene, demonstrating the sequential dissociation and chemisorption of the dissociated species on graphene induced by focused electron beam. (c)-(e) Experimental demonstration of chemisorption and physisorption of carbon adatoms deposited by the FEBID on graphene. (c) FEBID of carbon on graphene surface showing two regions where the primary electron (25 keV) directly irradiated for patterning squares and the secondary electron only affected to deposit carbon (surrounding the squares), whose surface topography and adsorption states were measured by the AFM imaging and the corresponding Raman D-band peak mapping. (d) The change of thickness after Raman laser-induced thermal ablation of the deposited carbon square structures indicating the fabrication of the molecularly thin carbon deposit film (~0.8 nm), and (e) the Raman I(D)/I(G) ratios upon laser-induced thermal ablation on two different regions confirming two different adsorption states of carbon on graphene. (Reprinted with permission from [33]. Copyright (2014) American Chemical Society)

X.4. Focused Electron Beam Induced Etching (FEBIE) of 2D Nanomaterials

Focused electron beam induced etching (FEBIE) is another mode of “direct-write” nanolithographic techniques

[34]. The FEBIE process can be applied to pattern inorganic and organic materials, for example, Ti, Si, SiO_2, Si_3N_4, GaAs, carbon nanomaterials and diamond, at high resolutions down to few nanometers with reactive gases such as H_2O, N_2, XeF_2, O_2, Cl_2 and NH_3 which are generally flooded into the SEM chamber through a gas injection nozzle with an inner diameter in an order of few hundreds micrometer [34, 35]. The gas molecule adsorbates are dissociated by secondary or backscattered electrons from the interaction of incident primary electrons with the target materials (substrates), and they turn into reactive radicals or ions and etch the target materials creating volatile compounds.

Carbon-based nanomaterials, *e.g.,* carbon nanotube, graphene and diamond, can be etched mostly with water vapors and oxygen gas under electron beam irradiation [34, 36-40]. Residual water vapors in the SEM chamber at the total pressure of 2×10^{-6} Torr were sufficient to cut multi-walled nanotubes under electron irradiation [36]. Figure 9(a) shows the TEM image showing a fine cutting (~40 nm) of the nanotube with a nominal beam spot size of ~3 nm. Water molecules were dissociated into highly reactive OH·, H· and HO_2· to react with carbon atoms forming volatile CO, CO_2 or hydrocarbon species. High partial pressure (2×10^{-5} Torr) of water led the etching process in the chemical reaction limited regime, where dissociation of water molecules became a dominant factor in etching carbon atoms, and thus, increasing the beam current at the fixed beam energy of 1 keV significantly reduced the cutting time of the nanotubes as shown in Fig. 9(b). In contrast, increasing the beam energy slowed down the cutting speed since the ionization cross section of water molecules is inversely proportional to the electron energy as shown in Fig. 10(c). These results conclude that the etching efficiency can be improved with a higher beam current and at a lower beam energy; however, the beam is broadened which can lower the etching resolution.

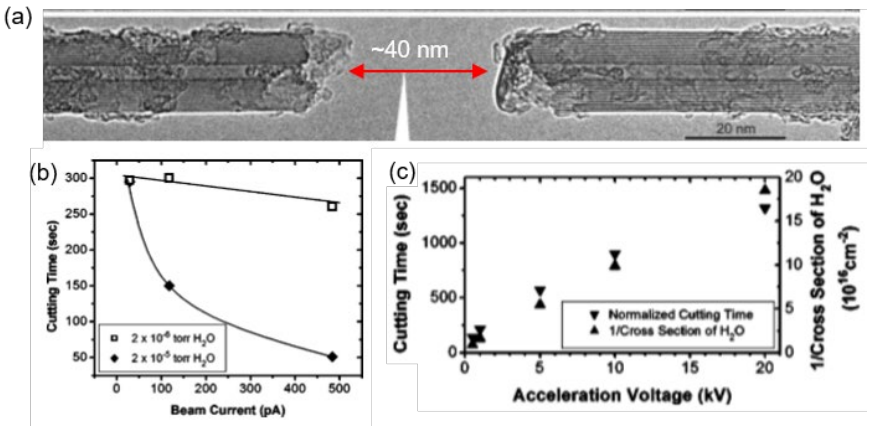

Figure 9. (a) TEM image of a multi-walled carbon nanotube etched by focused electron beam with residual water vapor, whose etching rate can be affected (b) proportionally by the electron beam current, but (c) inverse proportionally by the beam energy. (Reprinted from [36], with permission of AIP Publishing)

Suspended graphene can be also etched using FEBIE by directly injecting water vapors into the SEM chamber [37]. High resolution line etching with the cut width of ~7 nm was achieved with the high electron beam accelerating energy at 30 keV (nominal beam spot size of ~0.9 nm) as shown in Fig. 10(a). High resolution etching is also attributed to graphene's atomically thin layer whose interaction volume with the electron beam is limited leading to a very confined area of secondary/backscattered electron generations with the reduced yields. Using the FEBIE, suspended graphene nanoribbon was fabricated with a width of ~20 nm directly on the pre-fabricated graphene field-effect transistor, and the graphene nanoribbon was electrically measured showing a band gap energy of 60 meV. The supported graphene on an SiO_2/Si substrate was patterned using the 3 keV electron beam with oxygen gas molecules injected through a ~500 μm inner diameter nozzle (Fig. 10(b)), achieving tens of nanometer resolutions in a line etching mode as shown in Fig. 10(c) [38]. *In-situ* measurements of current during line cutting found the electron doses for the complete etch were ~8 mC/m and ~16 mC/m for a single-layer graphene and a bi-layer graphene, respectively, as shown in Fig. 10(d). In addition, the detailed study provided two underlying mechanisms of etching the supported graphene [38]. Imaging the intermediate state of graphene etching revealed that the etching started at the edges of graphene and continued to remove carbon atoms towards the center of the line. Also, the electron dose study of etching on the graphene basal plane revealed that, at a low electron dose (< 3 C/cm^2), hydrocarbon deposition occurred first due to initially high concentration of hydrocarbon surface contamination, and then the localized depletion of hydrocarbon contamination molecules allowed more adsorption sites of oxygen molecules to be available on the surface leading to etch hydrocarbon deposits and graphene when increasing the electron dose. These experimental findings highlight that leveraging surface contamination is of significance to improve the etching rate and resolution of the etched structures in the supported graphene. To improve the etching resolution, an inert N_2 gas was used: the ionized nitrogen interacting with the electron beam diffused onto the electron irradiation spot and etched carbon atoms on graphene. Since the ionized nitrogen is less reactive compared to water vapor or oxygen, finer control of etching was accomplished, which enabled the fabrication of sub-5 nm nanopores on suspended few-layer graphene with the focused electron beam at 5 keV [40].

Most of the FEBIE studies used a relatively large diameter injection nozzle, which leads to the flooding of a reactive gas in a free-molecular flow regime. Flooding of a reactive gas might contaminate the SEM chamber, increase the chamber resulting in greater e-beam scattering, and the non-interacting molecular flow of the gas does not enhance the outcomes of the FEBIE. To control the flow of a reactive gas, a micro-capillary nozzle with an inner diameter of 10 μm was used to deliver an oxygen gas in a continuum flow regime at a supersonic speed of the expanding gas jet, as shown in the schematic of the FEBIE process using a temperature-controlled oxygen micro-jet in Fig. 10(e) [39]. Modification of the oxygen gas flow provides an additional knob to control the FEBIE process. A localized oxygen supersonic micro-jet with the minimal jet spreading impinged on graphene surface at a high kinetic energy as described in the inset (Direct Simulation Monte Carlo result) of Fig. 10(e). Increasing oxygen jet temperature by heating the nozzle can additionally tune the FEBIE process *via* two physical mechanisms: (i) impact-stimulated activation of oxygen chemisorption on graphene, (ii) enhanced surface diffusion *vs.* desorption of hydrocarbon contamination molecules depending on the jet kinetic energy. Graphene

was etched free of parasitic halo deposits (common to FEBIP) using a supersonic oxygen micro-jet at ~30 times lower electron beam dose and even at the higher beam energy (10 keV) than using a conventional large diameter nozzle (500 μm) for delivery of oxygen. The heated micro-jet at 90 °C enabled faster etch of graphene as shown in Fig. 10(f), but enhanced the surface diffusion of hydrocarbon molecules which resulted in the faster growth of parasitic hydrocarbon deposits after the complete etch of graphene. This experiments suggest that the further improvement of graphene etching can be accomplished by high-temperature oxygen micro-jets whose impact kinetic energy is above the threshold for hydrocarbon molecule desorption.

Recently, a mechanically exfoliated few-layer MoS_2 channel in a field-effect transistor was successfully patterned using a pulsed focused electron beam induced etching with XeF_2 gas injected through a microneedle, as shown in Fig. 10(g) and 10(h) [41]. The etching process altered the doping status of a MoS_2 FET device which was evidenced by the blue-shifted threshold voltage indicating the change from n-type doping to more intrinsic or p-type doping. In addition, the field-effect mobility of the device was reduced from 1.96 $cm^2V^{-}s^{-}$ to 0.39 $cm^2V^{-}s^{-}$. The change of the electrical characteristics of the device was attributed to the formation of sulfur vacancies on the channel area, not directly exposed to the electron beam during the etch, and the atomic defects was also supported by micro-Raman and micro-photoluminescence spectroscopic measurements.

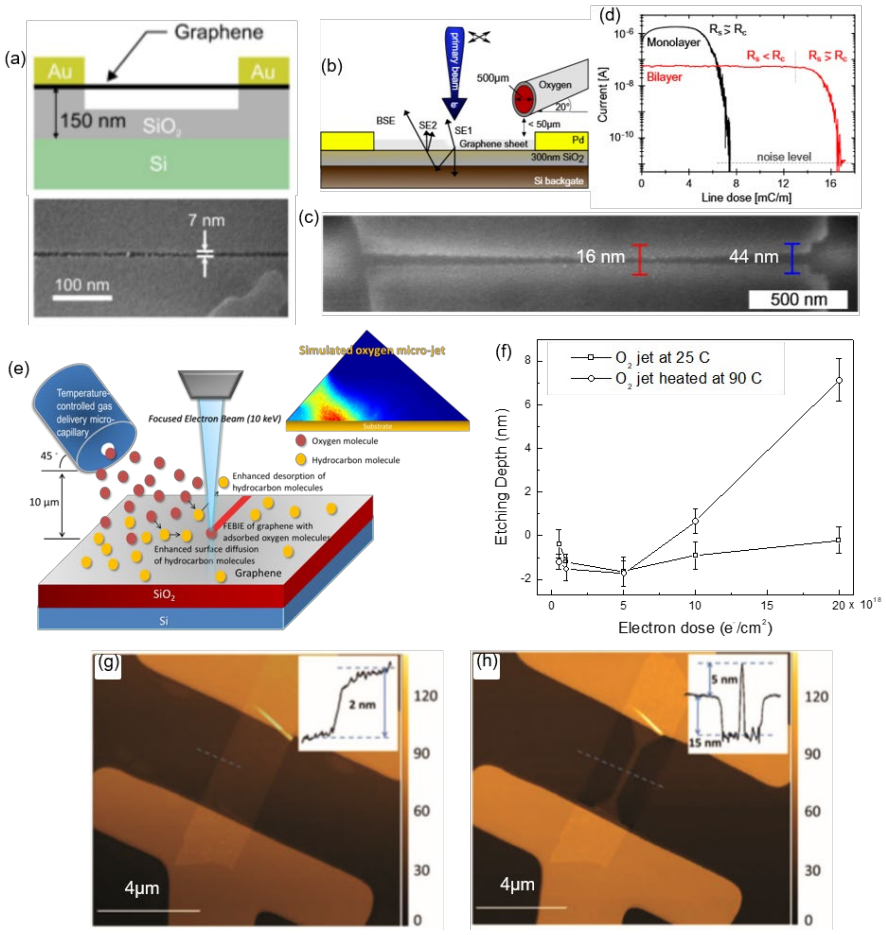

Figure 10. (a) FEBIE of suspended graphene showing 7 nm etching resolution with water vapor. (Reprinted by permission from Springer Nature Customer Service Centre GmbH: Springer Nature, Scientific Reports [37], Copyright (2015)) (b) Schematic showing the FEBIE set-up with a 500 μm inner diameter injection nozzle for flowing oxygen gas. (c) SEM images of line etch showing the tens of nanometer resolution on supported monolayer graphene and (d) the required electron doses for the complete etch of mono- and bi-layer graphene. (Reprinted from [38], Copyright (2013), with permission from Elsevier) (e) Schematic describing the FEBIE process with a micro nozzle (~10 μm inner diameter) to flow an oxygen supersonic micro-jet and (f) the etching outcomes of supported graphene with a room-temperature oxygen micro-jet and a heated micro-jet at 90 °C by increasing the electron doses. (Reprinted from [39], with permission of AIP Publishing) AFM images of a few-layer MoS_2 FET device (g) before and (h) after the channel was patterned. The insets show the heights of the channel. (Reproduced from Ref. 41 with permission from The Royal Society of Chemistry)

X.5. Applications of the FEBIP Techniques to 2D Nanomaterial-Based Electronic Devices

X.5.1. Nanoscale Welding

Focused electron beam induced deposition (FEBID) capability for site-specific, high-resolution patterning of nanomaterials was broadly utilized to enable a number of unique applications, including interfacial engineering of graphene-metal contacts, electromechanical welding of nanotubes, novel nanoscale electro-resistive or magnetic sensors, photonic and plasmonic devices [42]. One of the principal FEBIP appeals is in the local modifications of heterogeneous electrical contacts in low-dimensional nanomaterial-based electronic device structures. Weak couplings between low-dimensional nanomaterials and metal contacts is inevitable when developing electronic devices using the conventional lithography techniques such as metal evaporation or sputtering. Improving contact properties is a critical prerequisite to developing reliable, high-performance nanodevices by incorporation of many different types of low-dimensional nanomaterials into a composite opto-electro-magnetically active structure [43, 44]. Multi-walled carbon nanotubes (MWCNTs) were aligned on drain-source metal electrodes for electric interconnect applications, and both ends of the MWCNTs were electromechanically connected to the metal electrodes through graphitic contacts deposited by FEBID of carbon and annealed at 350 °C for ~ 30 min [43]. The successful, electrical connection of multiple inner shells of the MWCNTs to the metals reduced the device resistance down to the order of ~100 Ω from initially 1 GΩ. Similarly, thermo-electro-mechanical properties of graphene-metal interfaces were significantly enhanced after the nanoscale welding using the FEBID technique [44]. Figure 11(a) shows the nanoscale welding process of a graphene field-effect transistor using FEBID. A field-effect transistor was fabricated with the graphene channel underneath the metal source-drain contacts. The graphene-metal contacts of the as-fabricated device have poor interfacial properties due to their intrinsically weak interaction as well as PMMA lithographic polymer residues. The buried interfaces were engineered by irradiating a focused electron beam at graphene-metal contact areas,

and the high energy electrons traveled through the metal contacts to be accessible for modifying the interfacial properties in two mechanisms; generation of sp^3-type defects on graphene and chemical interconnection of graphene and metal with the electron beam dissociated carbon/graphitic layers. Transport characteristics of the graphene FETs before and after the interfacial engineering verified that the FEBID nanoscale welding process improved thermo-mechanical properties of the interfaces with the reduction of device resistances by ~50% at a Dirac point and by ~30% at the gate voltage far from the Dirac point as shown in Figs. 11(b) and 11(c), and the mechanism of the improvements was revealed experimentally by Raman spectroscopic and AFM analysis.

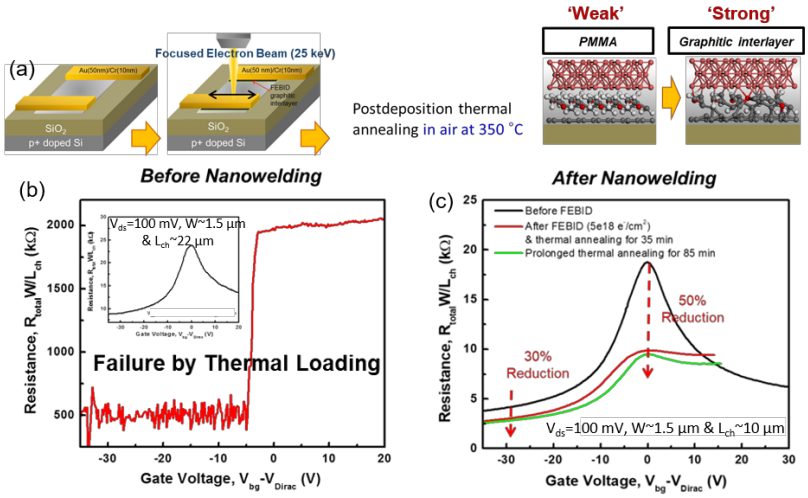

Figure 11. (a) Schematic describing the nanoscale welding process of graphene-metal interfaces using the FEBID. Two-terminal electrical resistance measurements of graphene devices by changing the gate voltage demonstrating that (b) the as-fabricated device with no nanoscale welding was failed by thermal loading, but (c) the significant improvement of interfacial properties of graphene-metal contacts was achieved with the nanoscale welding process. (Adapted with permission from [44]. Copyright (2016) American Chemical Society)

X.5.2. Reconfigurable Graphene Doping

Modulation of doping levels in graphene nanoelectronic devices is useful to control device functionalities and performance. P-type doping of graphene can be easily realized by water molecule adsorption and polymer resist residual during wet-transfer of graphene and lithography procedures for device fabrication [45]. However, n-type doping requires multiple steps of treatments such as plasma treatment, electro-thermal reaction, chemical treatment for surface adsorption of n-type dopants or electron beam irradiation [46]. Controlled, localized n-type doping was demonstrated during the FEBID [46]. Figure 12(a) shows the strategy for the controlled n-type doping of the channel on a graphene field-effect transistor. The controlled electron dose of a primary beam on graphene-metal contact areas varied the number of secondary electrons generated from the long-traveling primary electrons

(backscattered electrons escaping from the graphene channel area), and resultantly, changed the coverage of carbon deposition (doping) on the channel area which was deposited from the source of hydrocarbon contamination molecules. Increasing the electron dose led to the change of the doping level from p-type doping (pristine) to n-p-n doping at a low dose (10^{18} electron/cm^2) and n-type doping at a high dose (10^{19} electron/cm^2), as shown in Fig. 12(b). More interestingly, diffusion and redistribution of weakly interacting FEBID carbon atoms on graphene towards the low-concentrated area on the graphene channel reconfigured the doping state to the p-type doping as shown in Fig. 12(c). This work highlights the capability of the FEBID technique for development of dynamically reconfigurable graphene devices.

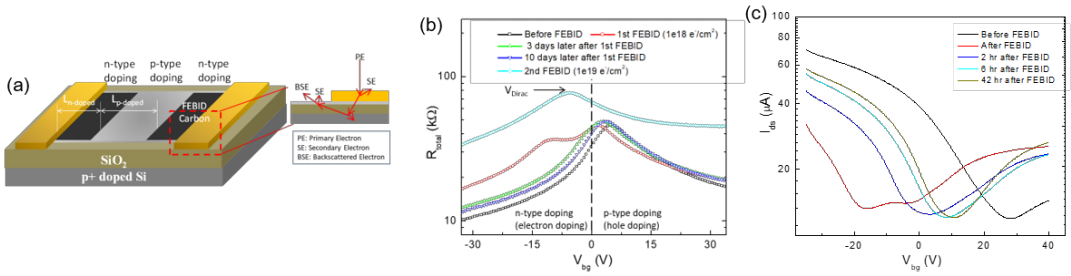

Figure 12. (a) Schematic showing the carbon doping process on a graphene device using the FEBID technique. (b) Electrical measurement results showing the controllability of graphene doping states from n-p-n junction formation to fully n-type doping by controlling the electron beam dose and (c) the reconfigurable doping state which is transiently changed from the n-p-n doping state to the p-type doping by the diffusion and redistribution of carbon adatoms on graphene surface. (Reproduced from Ref. 46 with permission from The Royal Society of Chemistry)

Direct irradiation of a graphene channel in a FET device by high-energy primary electrons can also control doping states as a result of the electron beam-induced modulation of the charge distribution on the SiO_2 substrate [47]. The site-specific reversible bipolar graphene doping was achieved by changing an accelerating energy of a primary beam as shown in Fig. 13(b). Irradiation at a low beam energy induced n-type doping and increasing the beam energy led to a transition from n-type (Dirac point at -55 V after 2 keV electron irradiations) to p-type doping (11 V after 30 keV electron irradiations). *In-situ* electrical measurement set-up in the SEM allowed for observing the swift change of the doping state from n-type to p-type doping (and vice versa) by altering the beam energies. "Write-erase" cycles (Fig. 13(c)) were programmable up to 10^4 cycles owing to the relatively low electron dose required for changing doping levels, and finally, an electron beam-driven programmable graphene logic devices were demonstrated for NAND and OR gates, as shown in Fig. 13(d). The developed technique was also applied to a MoS_2 FET device, and the similar effect of electron beam irradiation on a MoS_2 channel was observed at 2 keV. Clearly distinguishable 'ON' and 'OFF' states were demonstrated by being exposed to the electron beam at 2 keV and 30 keV, respectively.

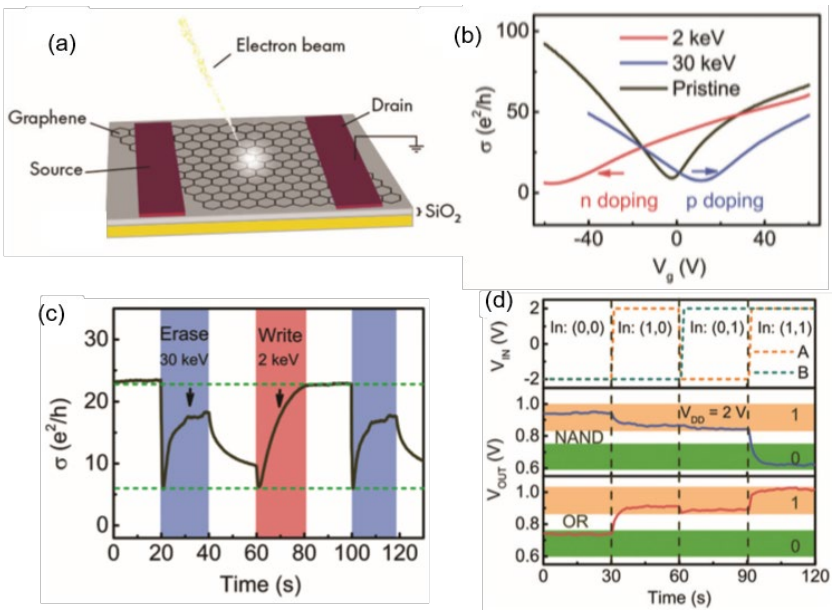

Figure 13. (a) Schematic describing the direct irradiation of a graphene channel using a primary electron beam for the controlled modulation of graphene doping states. (b) Conductivity measurement results by modulating gate voltages demonstrating the capability of the site-specific bipolar graphene doping using the direct primary electron irradiation with different beam energies which enables (c) the realization of "writing" and "erasing" modes of the graphene device and (d) the development of graphene-based logic devices such as NAND and OR gates. (Reproduced from Ref. 47 with permission from The Royal Society of Chemistry)

X.5.3. Tuning MoS_2-Based Nanoelectronic Devices

The representative inorganic 2D nanomaterial is a single- or few-layered MoS_2 which is a semiconductor and whose semiconducting phase (2H-MoS_2) can be transformed to a metallic phase (1T-MoS_2) by external energy deposition [13, 48]. Electron beam irradiation can controllably convert the phase of MoS_2 site-specifically and allows for the fabrication of an atomically thin lateral 2H/1T Schottky junctions and SB-FETs [49, 50]. Figures 14(a) and 14(b) show the schematic of 1T/2H Schottky junction fabrication on few layer n-type MoS_2 flakes by electron beam irradiation and the optical microscope image of the devices along with the schematic of a final device structure [49]. The electron dose of 10^{20} electrons/cm^2 was not enough for phase transition, but the increase of the dose to 1.6×10^{20} electrons/cm^2 provoked the formation of a 1T metallic phase at room temperature. The electrical measurements of the fabricated in-plane SB-FETs in Fig. 14(c) demonstrated the formation of a Schottky junction which showed the clear asymmetric behavior (rectification property), while the symmetric I-V curve was measured for the device with no Schottky junction as shown in Fig. 14(d).

A CVD monolayer MoS_2 (Fig. 15(a)) was also investigated to study the effect of electron beam irradiation on its transport properties and a photoelectric performance of a MoS_2 device shown in Fig. 15(b) [51].

The elemental analysis of the monolayer MoS_2 was conducted using X-ray photoelectron spectroscopy (XPS) before and after electron irradiation at 10 keV for 10 min. The results demonstrated the change of stoichiometry from 1.84:1 to 1:1.65 for S:Mo, which is indicative of S vacancy formation. Electron beam irradiation reduced the source-drain current and the field-effect mobility of the devices with an on/off current ratio unchanged, which were measured in air. However, the photoelectric performance of the device was improved after irradiation. The light response and release time were significantly reduced from 11 s and 105 s to 6 s and 5 s, respectively, as shown in Figs. 15(c) and 15(d). The light dark current ratio also increased from 7.6 s to 34.6 s. The improvement of the photoelectric performance was due to the defect-assisted electron-hole recombination, which was revealed by Kelvin Probe Force Microscopy (KPFM) measurements.

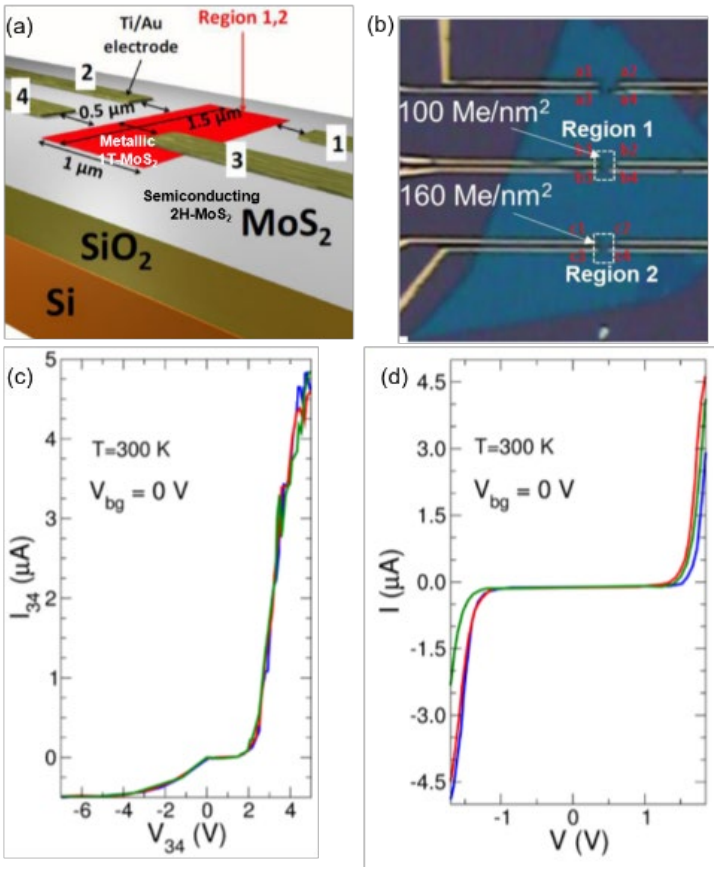

Figure 14. (a) Schematic view of few-layer MoS_2 devices with electron beam-induced Schottky junction formation and (b) the optical microscope image of the devices. I-V measurements of the devices irradiated with the electron dose of (c) 1.6×10^{20} electrons/cm^2 (Schottky junction formation) and (d) 10^{20} electrons/cm^2 (no Schottky junction formation). (Reprinted with permission from [49]. Copyright (2016) American Chemical Society)

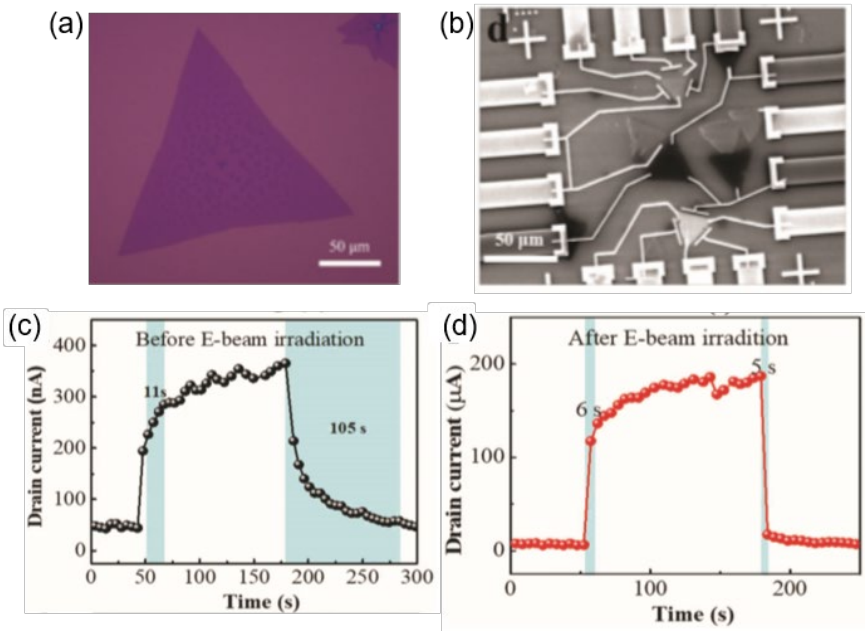

Figure 15. (a) Optical microscope image of a CVD-grown single-layer MoS_2 on the SiO_2/Si substrate, and the SEM image of the MoS_2 device with the Ti/Au contacts. The drain current measurements with light on and off for the device (c) before and (d) after electron beam irradiation, which shows the enhanced photoelectron property with electron beam induced modification of MoS_2 ([51] John Wiley & Sons. © 2018 WILEY-VCH Verlag GmbH & Co. KGaA, Weinheim)

X.6. End-of-Chapter Conclusion

This chapter discusses the scientific bases and showcases the multi-modal nanofabrication capabilities of FEBIP as a next-generation lithography technique, with specific focus on processing of 2D organic and inorganic nanomaterials. From atomic scale opto-electro-mechanical and chemical property modification to enabling communication and quantum information applications, FEBIP holds promise in local physicochemical engineering of nanomaterials and fabrication of unique device architectures combining 1D, 2D and 3D topologies with unprecedented resolution and functional feature control at the heterogeneous material interfaces. Importantly, in the realm of 2D atomically thin materials, which are highly sensitive to contamination and material handling in between of processing steps, FEBIP exceed the capabilities of conventional lithography methods by enabling the multi-step fabrication of composite nanodevices within the same processing environment. Using the standard toolbox of an electron microscope but in combination with on-demand reconfigurable chemical precursor injection system allows for all the steps required for fabrication of a fully functional nano-opto/electro/mechanical device accomplished in the same chamber without ever breaking vacuum. These include structural element functionalization/defect formation/doping; definition and geometrical patterning (*via* etch process by FEBIE); metal/metal oxide coating (*via* deposition process by FEBID); interface fusion and activation, active channel cleaning from parasitic adsorbates and changing the 2D layer redox state with atomic resolution.

X.7. Student's Corner

FEBIP capabilities are particularly compelling to enrich the material processing capabilities and to create new nano-system architectures in the emerging field of quantum computing and information processing. The next frontier in FEBIP as a nanolithography tool of 2D materials is exploration for the use of liquid phase precursors to enable new (electro)chemical modes of material processing using solvated electrons and highly reactive radiolytic species, which enable an extension of patterning topologies from conventional 2D line and dot structures on the surface to 3D bridges and overpasses over the surface [52, 53]. The use of a cryogenic cooling provides another promising route for expanding the FEBIP capabilities by taking an advantage of the condensed state of the precursor forming a thin low-mobility "frozen" layer on a substrate for improved control of processing outcomes [54].

Recent advances in technological capabilities of FEBIP, including development of CAD tools [55] for *in silico* process design, enable both device architects to develop new concepts of nanomaterials or functional systems and basic science researchers to conduct fundamental research on 2D material behavior with the *in-situ* imaging capability, exploring new physical phenomena that are triggered by local perturbation of the material state on a single atom scale. From the manufacturing perspective, the FEBIP is currently most suitable for laboratory scale "prototyping" the new concepts of 2D nanomaterials and devices. "Direct-write" nature of FEBIP is cost (and processing time) prohibitive for large-scale production, which is possible with the conventional batch semiconductor processing. Potentially, the FEBIP scale-up to wafer-level can be achieved with continuous development of instrumentation and reduction of the process time, such as massively parallel multi-beam systems as well as process automation, which can be realized with the faster control hardware for electron beam and gas injection coupled to the real-time monitoring and image data analytics through an instant feedback system.

ACKNOWLEDGEMENTS

This book chapter was supported by the U.S. Department of Energy (DOE), Office of Science, Basic Energy Sciences (BES), under Award #DE-SC0010729 and by the National Research Foundation of Korea (NRF) grant funded by the Korea government (MSIT) (No. 2019R1C1C1010556).

REFERENCES

[1] Zhang H 2015 ACS Nano 9(10) 9451-9469

[2] Novoselov K S, Geim A K, Morozov S V, Jiang D, Zhang Y, Dubonos S V, Grigorieva I V and Firsov A A 2004 Science 306(5696) 666-669

[3] Geim A K and Grigorieva I V 2013 Nature 499(7459) 419-425

[4] Sun L T, Banhart F and Warner 2015 J MRS Bull. 40(1) 29-37

[5] Zhao X, Kotakoski J, Meyer J C, Sutter E, Sutter P, Krasheninnikov A V, Kaiser U and Zhou W 2017 MRS

Bull. 42(9) 667-676.
[6] Banhart F, Kotakoski J and Krasheninnikov A V 2011 ACS Nano 5(1) 26-41
[7] Li L, Reich S and Robertson J 2005 Phys. Rev. B. 72(18) 184109
[8] Robertson A W and Warner J H 2013 Nanoscale 5(10) 4079-4093
[9] Zhao J, Deng Q, Bachmatiuk A, Sandeep G, Popov A, Eckert J and Rummeli M H 2014 Science 343(6176) 1228-1232.
[10] Wei X L, Wang M-S, Bando Y and Goldberg D 2011 ACS Nano 5(4) 2916-2922
[11] Zobelli A, Gloter A, Ewels C P, Seifert G and Colliex C 2007 Phys. Rev. B. 75(24) 245402
[12] Komsa H P, Kotakoski J, Kurasch S, Lehtinen O, Kaiser U and Krasheninnikov A V 2012 Phy. Rev. Lett. 109(3) 035503
[13] Lin Y C, Dumcenco D O, Huang Y S and Suenaga K 2014 Nat. Nanotechnol. 9(5) 391-396
[14] van der Zande A M, Huang P Y, Chenet D A, Berkelbach T C, You Y M, Lee G H, Heinz T F, Reichman D R, Muller D A and Hone J C 2013 Nat. Mater. 12(6) 554-561
[15] Wang S S, Lee G D Lee S Yoon E and Warner J H 2016 ACS Nano 10(5) 5419-5430
[16] Lin J H, Cretu O, Zhou W, Suenaga K, *et al.* 2014 Nat. Nanotechnol. 9(6) 436-442
[17] Kalinin S V, Borisevich A and Jesse S 2016 Nature 539(7630) 485-487
[18] Susi T, Kepaptsoglou D, Mangler C, Lovejoy T C, Krivanek O L, *et al.* 2014 Phys. Rev. Lett. 113(11) 115501
[19] Dyck O, Kim S, Jimenez-Izal E, Alexandrova A N, Kalinin S V and Jesse S 2018 Small 14(38) 1801771
[20] Su C, Tripathi M, Yan Q B, Wang Z, et al. 2019 Sci. Adv. 5(5) eaav2252
[21] Ziatdinov M, Dyck O, Jesse S and Kalinin S V 2019 Adv. Funct. Mater. 29 1904480
[22] Kulkarni D D, Kim S, Chyasnavichyus M, Hu K, Fedorov A G and Tsukruk V V 2014 J. Am. Chem. Soc. 136(18) 6546-6549
[23] Dreyer D R, Park S, Bielawski C W and Ruoff R S 2010 Chem. Soc. Rev. 39(1) 228-240
[24] Kim S, Kulkarni D D, Henry M, Zackowski P, Jang S S, Tsukruk V V and Fedorov A G 2015 Appl. Phys. Lett. 106(13) 133109
[25] Jones J D, Mahajan K K, Williams W H, Ecton P A, Mo Y and Perez J M 2010 Carbon 48(8) 2335-2340
[26] Withers F, Bointon T H, Dubois M, Russo S and Craciun M F 2011 Nano Lett. 11(9) 3912-3916
[27] Zhou Y G, Wang Z G, Yang P, Zu x T, Xiao H Y, Sun X, Khaleel M A and Gao F 2011 Phys. Chem. Chem. Phys. 13(37) 16574-16578
[28] Balakrishnan J, Koon G K W, Jaiswall M, Castro Neto A H and Ozyilmaz B 2013 Nat. Phys. 9(5) 284-287.
[29] Lee W K, Whitener K E, Robinson J T and Sheehan P E 2015 Adv. Mater. 27(10) 1774-1778
[30] Ryu S, Han M Y, Maultzsch J, Heinz T F, Kim P, Steigerwald M L and Brus L E 2008 Nano Lett. 8(12) 4597-4602
[31] Feng W, Long P, Feng Y and Li Y 2016 Adv. Sci. 3(7) 1500413
[32] Martins S E, Withers F, Dubois M, Craciun M F and Russo S 2013 New J. Phys. 15 033024
[33] Kim S, Kulkarni D D, Davis R, Kim S S, *et al.* 2014 ACS Nano 8(7) 6805-6813
[34] Toth M 2014 Appl. Phys. A. 117(4) 1623-1629
[35] Schoenaker F J, Cordoba R, Fernandez-Pacheco R, Magen C, Stephan O, Zuriaga-Monroy C, Ibarra M R

and De Teresa J M 2011 Nanotechnology **22**(26) 265304

[36] Yuzvinsky T D, Fennimore A M, Mickelson W, Esquivias C and Zettl A 2005 Appl. Phys. Lett. 86(5) 053109

[37] Sommer B, Sonntag J, Ganczarczyk A, Braam D, Prinz G, Lorke A and Geller M 2015 Sci. Rep. 5. 7781

[38] Thiele C, Felten A, Echtermeyer T J, Ferrari A C, Casiraghi C, Lohneysen H and Krupke R 2013 Carbon 64 84-91.

[39] Kim S, Henry M and Fedorov A G 2015 Appl. Phys. Lett. 107(23) 233102

[40] Fox D S, Maguire P, Zhou Y, Rodenburg C, O'Neill A, Coleman J N and Zhang Hongzhou 2016 Nanotechnology 27(19) 195302

[41] Urbanos F J, Black A, Rbernardo-Gavito R, Vazquez de Parga A L, Miranda R and Granados D 2019 Nanoscale 11(23) 11152-11158

[42] Huth M, Porrati F and Dobrovolskiy O V 2018 Microelectron. Eng. 185 9-28

[43] Kim S, Kulkarni D D, Rykaczewski K, Henry M, Tsukruk V V and Fedorov A G 2012 IEEE Trans. Nanotechnol. 11(6) 1223-1230

[44] Kim S, Russell M, Kulkarni D D, Henry M, *et al.* 2016 ACS Nano 10(1) 1042-1049

[45] Shin D W, Lee H M, Yu S M, Lim K S, *et al.* 2012 ACS Nano 6(9) 7781-7788

[46] Kim S, Russell M, Henry M, Kim S S, *et al.* 2015 Nanoscale 7(36) 14946-14952

[47] Zhou Y B, Jadwiszczak J, Keane D, Chen Y, Yu D and Zhang H 2017 Nanoscale 9(25) 8657-8664

[48] Kappera R, Voiry D, Yalcin S E, Branch B, Gupta G, Mohite A D and Chhowalla M 2014 Nat. Mater. 13(12) 1128

[49] Katagiri Y, Nakamura T, Ishii A, Ohata C, *et al.* 2016 Nano Lett. 16(6) 3788-3794

[50] Katagiri Y, Nakamura T, Ohata C, Katsumoto S and Haruyama J 2017 Appl. Phys. Lett. 110(14) 143109

[51] Li F, Gao F, Xu M, Liu X, Zhang X, Wu H and Qi J 2018 Adv. Mater. Interf. 5(14) 1800348

[52] Fisher J, Kottke P A, Kim S and Fedorov A G 2015 Nano Lett. 15(12) 8385-8391

[53] Fisher J, Kottke P A and Fedorov A G 2018 Mater. Today Phys. 5 87-92

[54] Cordoba R, Orus P, Strohauer S, Torres T E and De Teresa J M 2019 Sci. Rep. 9 14076

[55] Fowlkes J D, Winkler R, Lewis B B, Fernández-Pacheco A, *et al.* 2018 ACS Appl. Nano Mater. 1 1028-1041